Passive Tomography of Turbulence Strength

Marina Alterman[1], Yoav Y. Schechner[1],
Minh Vo[2], and Srinivasa G. Narasimhan[2]

[1] Dept. Electrical Eng., Technion - Israel Institute of Technology, Haifa, Israel
[2] Robotics Institute, Carnegie Mellon University, Pittsburgh, PA, USA

Abstract. Turbulence is studied extensively in remote sensing, astronomy, meteorology, aerodynamics and fluid dynamics. The strength of turbulence is a statistical measure of local variations in the turbulent medium. It influences engineering decisions made in these domains. Turbulence strength (TS) also affects safety of aircraft and tethered balloons, and reliability of free-space electromagnetic relays. We show that it is possible to estimate TS, without having to reconstruct instantaneous fluid flow fields. Instead, the TS field can be directly recovered, passively, using videos captured from different viewpoints. We formulate this as a linear tomography problem with a structure unique to turbulence fields. No tight synchronization between cameras is needed. Thus, realization is very simple to deploy using consumer-grade cameras. We experimentally demonstrate this both in a lab and in a large-scale uncontrolled complex outdoor environment, which includes industrial, rural and urban areas.

1 The Need to Recover Turbulence Strength

Turbulence creates refractive perturbations to light passing through a scene. This causes random distortions when imaging background objects. Hence, modeling and trying to compensate for random refractive distortions has long been studied in remote sensing [40], astronomy [34] and increasingly in computer vision [2,4,10,14,18,35,38,41,52,55]. Nevertheless, these distortion are not necessarily a problem: they offer information about the medium and the scene itself [44]. This insight is analogous to imaging in scattering media (fog [29], haze [19,37], water [11,30]), where visibility reduction yields ranging and characterizing of the medium. Similar efforts are made to reconstruct refracting (transparent) solids or water surfaces [3,16,28,43,46] from images of a distorted background or light field [50,51]. In turbulence, refraction occurs continuously throughout a volume.

We *exploit* random image distortions as a means to estimate the spatial (volumetric) distribution of *turbulence strength* (TS). The strength of turbulence is a statistical measure of local variations in the medium [20,21]. Often, it is not necessary to estimate an instantaneous snapshot of air density or refraction field [32,42]. Rather *local statistics* is relied upon heavily in many applications. Meteorologists rely on TS to understand convection (which forms clouds), wind, and atmospheric stability. This is measured using special Doppler lidars [9,31], which are very expensive. Turbulence significantly affects the efficiency of wind

turbine farms [31], hence optimizing turbines and farms involves measuring TS. Similarly, the design and performance of other aerodynamic objects (wings, winglets, jets engines etc.) is tied to the strength of the non-laminar flow around them. In such cases, the statistics of the flow field are important, as they convey transfer of energy, loads, correlations and spatiotemporal spectra. The TS is also an indicator for gliding birds who use convection for lift. Moreover, determining which areas have stronger or weaker turbulence can optimize free-space optical relay of communication and power [31].

One might estimate TS using many consecutively recovered instantaneous refractive fields [33,47,48]. These instantaneous fields may themselves be estimated by multiview tightly-synchronized image sequences. Indeed, several works recover time-varying 3D gas flows [6,7,52]. However, there are advantages for measuring the TS directly, without recovering instantaneous fields. Estimating an instantaneous refractive field may be ill-posed [7] or require more complex setups involving active light-field probes [17,39]. In addition, direct estimation of the TS avoids any propagation of errors stemming from inaccurate instantaneous fields. TS is passively estimated in [54] assuming a path-constant (uniform) TS rather than a spatially varying field. Another related work is [44]. There, spatially stationary turbulence is exploited to estimate object range.

In this paper, we describe how the TS field can be directly estimated using only passive multiview observations of a background. The variances in image projections of background features are computed by tracking those features over a few hundred frames. The variance at each pixel at each camera viewpoint is simply a weighted integral of the TS field along the respective pixels' line of sight (LOS). The LOSs of all pixels from all viewpoints crisscross the turbulence field. Estimating the TS's volumetric distribution is then equivalent to solving a linear tomography problem. While linear tomography is common in medical imaging, the specific structure here is different. Thus, our domain and model form a new addition to the set of tomographic problems, which recently raise interest in computational photography and vision [1,7,13,26,27,36,46,51].

We demonstrate our model and method using experiments indoors and outdoors, as well as simulations. Outdoors, we estimate the TS field in a large scale: a city, in a complex terrain including urban, industrial and rural areas. We believe this is the first attempt to reconstruct such a large field passively.

2   Theoretical Background

2.1   Turbulence Statistics and Refraction

The refractive index of air $n(\mathbf{X}, t)$ at spatial location $\mathbf{X} = (X, Y, Z)$ and time t is a function of various meteorological parameters (air pressure, temperature, humidity etc.). Due to random spatiotemporal fluctuations of these parameters, $n(\mathbf{X}, t)$ is random in space and time. Temporally stationary atmospheric turbulence is characterized by a *structure function* for refractive index fluctuations. The refractive index structure function [22,44] is

$$\mathcal{D}_n(\mathbf{X}_1, \mathbf{X}_2) = \langle [n(\mathbf{X}_1, t) - n(\mathbf{X}_2, t)]^2 \rangle_t. \tag{1}$$
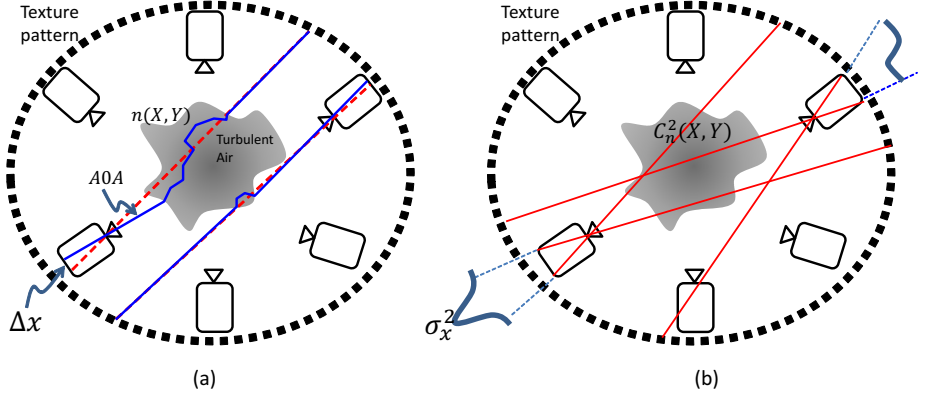
Fig. 1. Multiple cameras are placed around a chunk of turbulent air. (a) An object point of a textured pattern projects to a camera pixel through air having a spatially varying refractive index. (b) Temporal variance of pixel displacement of a textured object is associated to a pixel. This yields data for linear tomography of the statistical field C_n^2.

It represents the mean squared difference of refractive indices at different locations $\mathbf{X}_1$ and $\mathbf{X}_2$. When the structure function depends only on the distance $\rho = ||\mathbf{X}_1 - \mathbf{X}_2||$, Kolmogorov [20,21] showed that

$$\mathcal{D}_n(\rho) = C_n^2 \rho^{2/3}. \tag{2}$$

Here C_n^2 is the refractive index structure constant [22,44]. The parameter C_n^2 expresses TS. High values of C_n^2 imply strong turbulence, while $C_n^2 = 0$ means that the air is not turbulent.[1] The TS changes spatially, thus we denote it $C_n^2(\mathbf{X})$.

There is an LOS between a background object point and a camera at distance L away. Without turbulence, the LOS has an angle of arrival (AOA) relative to the optical axis. Fluctuations of the atmospheric refractive index lead to random refractions of propagating light (see Fig. 1a). Hence turbulence perturbs the LOS. To gain intuition, consider an object point that radiates to all directions, and an atmosphere which is not turbulent, other than a single thin phase screen. A phase screen represents a layer having spatiotemporal $n(\mathbf{X}, t)$. At any t the phase screen randomly deviates the direction of each incoming ray, once. Suppose the phase screen is just adjacent to the object point. In this case, the direction of rays emanating from the point are randomly permuted. Nevertheless, overall rays appear to radiate in all directions, just as a point source without turbulence. Hence, in this case, the turbulent layer does not affect the image.

On the other hand, suppose the phase screen is adjacent to the camera's exit pupil. A ray between the object and the pupil varies its direction as it passes

---

[1] The distance ρ is in units of m. Then, the units of C_n^2 are $m^{-2/3}$. Typical values of C_n^2 are in the range $10^{-17} - 10^{-13}$ $m^{-2/3}$.

the phase-screen. The ray thus enters the camera at a different AOA, leading to a distorted projection. These two special cases imply that turbulence affects an image, depending both on the TS value in a voxel, and the distance of the voxel along any LOS. The entire 3D field can be modeled by a series of phase screens, each perturbing the propagation direction. This is analogous to a random walk of any ray between the object and the pupil. For a wide-angle radiating source (a point source), models established in the literature [22,44] express the variance σ_{AOA}^2 of the AOA by integration along the LOS

$$\sigma_{\mathrm{AOA}}^2 = 2.914D^{-1/3} \int_0^L C_n^2[\mathbf{X}(s)] \left(\frac{s}{L}\right)^{5/3} ds, \qquad \mathbf{X} \in \mathrm{LOS}. \tag{3}$$

Here D is the camera aperture diameter, $s = 0$ corresponds to the background object location, while $s = L$ corresponds to the lens pupil location.

2.2   Linear Tomography

A linear emission tomography model typically applies to independent emitters, e.g., fluorescent molecules and radioactive probes used in SPECT. A volumetric field $e(\mathbf{X})$ of emitters is projected by a camera at some pose. Pixel $\mathbf{p}$ then corresponds to a particular LOS, denoted $\mathrm{LOS_p}$. Parameterize a position on $\mathrm{LOS_p}$ by $s \in [0, L]$. Set $s = 0$ at a background point, while $s = L$ corresponds to the lens pupil. The measured intensity at $\mathbf{p}$ is then the line integral
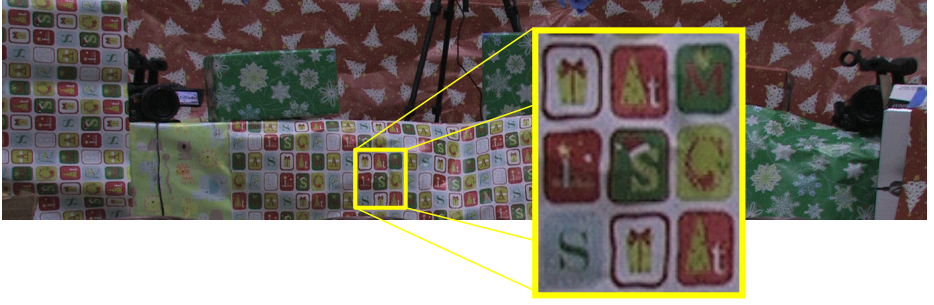
$$I(\mathbf{p}) \propto \int_0^L e[\mathbf{X}(s)]ds, \qquad \mathbf{X} \in \mathrm{LOS_p}. \tag{4}$$

Different LOSs can provide independent linear equations as (4). Based on these equations, $e(\mathbf{X})$ can be estimated $\forall \mathbf{X}$. The line integral in Eq. (4) is insensitive to flipping of the coordinate system (counter propagation): if the pupil moves to $s = 0$ while the background point is at $s = L$, Eq. (4) yields the same value. Hence, in typical linear emission tomography, it suffices to measure $I(\mathbf{p})$ from half the directional domain.

3   Principle of C_n^2 Tomography

As seen in Eq. (3), a single LOS is perturbed by a path-averaged $C_n^2(\mathbf{X})$. By utilizing *several* viewpoints, it may be possible to recover the spatial distribution $C_n^2(\mathbf{X})$ based on Eq. (3). This is a new field for linear tomography. Data on σ_{AOA}^2 can be obtained by analyzing either AOA fluctuations [54] for short exposures or image blur for long exposures, at scene features of known range. Here too, pixel $\mathbf{p}$ corresponds to $\mathrm{LOS_p}$. Using Eqs. (3,4), the measured AOA variance at $\mathbf{p}$ is

$$\sigma_{\mathrm{AOA}}^2(\mathbf{p}) \propto \int_0^L C_n^2[\mathbf{X}(s)]s^{5/3}ds, \qquad \mathbf{X} \in \mathrm{LOS_p}. \tag{5}$$

Fig. 2. An example of an image frame as seen through turbulent air. Notice the distorted edges in the magnified region.

Analogously to Sec. 2.2, different LOSs can provide independent linear equations as (5), relating the unknown field C_n^2, to the measured σ_{AOA}^2. Based on these equations, $C_n^2[\mathbf{X}(s)]$ can be estimated $\forall \mathbf{X}$. However, contrary to linear emission tomography, the line integral in Eq. (5) is *sensitive* to flipping the coordinate system (counter propagation): voxels closer to the camera have more weight in Eq. (5), than distant voxels (for which $s \to 0$). Thus, counter-directions yield independent measurements.

3.1   Numeric Tomographic Recovery of C_n^2

Consider the setup in Fig. 1(a). The background is a textured pattern. Multiple cameras are placed around a chunk of air. An object point projects to pixel

$$x = f \tan \text{AOA}, \tag{6}$$

where f is the focal length of the camera. Due to turbulence, random image distortions are observed over time. Each temporal frame is spatially distorted (in Fig. 2, notice the distorted edges in the magnified region). The image pixel displacement has variance

$$\sigma_{\mathbf{x}}^2 \approx f^2 \left[\frac{d \tan(\text{AOA})}{d\text{AOA}} \right]^2 \sigma_{\text{AOA}}^2 = f^2 \frac{1}{\cos^4(\text{AOA})} \sigma_{\text{AOA}}^2. \tag{7}$$

Later, in Sec. 5.1, we describe an experiment in which air is heated by electric griddles, creating turbulence that distorts a background texture. Fig. 3 shows displacement variance maps from different viewpoints. High variance in the map means that a LOS passes through more turbulence, than at pixels exhibiting low displacement variance.

As illustrated in Fig. 4, we discretize the volume domain into a 3D grid of voxels $\{V_k\}_{k=1}^{N_{\text{voxels}}}$. Without turbulence, pixel $\mathbf{p}$ observes object point $\mathbf{O}$ through
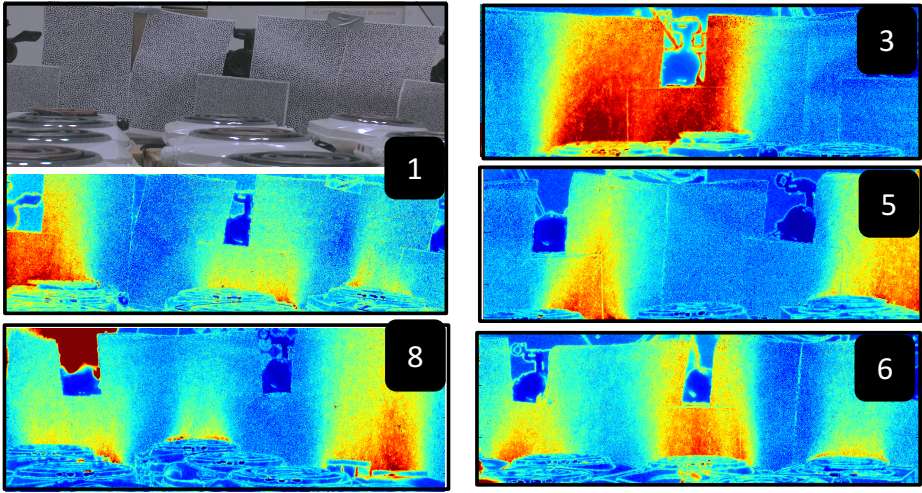
Fig. 3. Sample variance images from an experiment corresponding to Fig. 6. A textured pattern which is placed behind the stove is shown aligned with its variance image, from one view. Sample variance images of pixel displacements, in various views, with corresponding camera indices. Red expresses high variance while blue represents low variance. High variance regions appear only behind hot stoves.
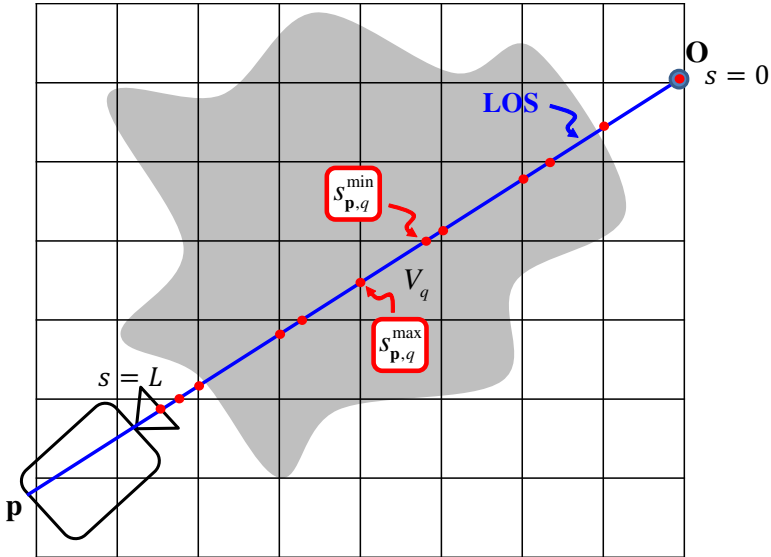
Fig. 4. The volume is discretized into voxels. The LOS intersects voxel V_q at points $s_{\mathbf{p},q}^{\min}$ and $s_{\mathbf{p},q}^{\max}$. The voxel intersection points $\Psi_{\mathbf{p},q} \equiv \mathrm{LOS}_{\mathbf{p}} \cap V_q$ are used as weights in the LOS integration (9).

$\text{LOS}_{\mathbf{p}}$. Let $\text{LOS}_{\mathbf{p}}$ intersect voxel V_q. The line intersection is $\Psi_{\mathbf{p},q} \equiv \text{LOS}_{\mathbf{p}} \cap V_q$. It is bounded by two points,[2] at corresponding distances from $\mathbf{O}$:

$$s_{\mathbf{p},q}^{\min} = \min_{\mathbf{X} \in \Psi_{\mathbf{p},q}} \|\mathbf{X} - \mathbf{O}\| \qquad\qquad s_{\mathbf{p},q}^{\max} = \max_{\mathbf{X} \in \Psi_{\mathbf{p},q}} \|\mathbf{X} - \mathbf{O}\|. \qquad (8)$$

Approximate C_n^2 as constant in each voxel. Based on Eqs. (3,7,8),

$$\sigma_{\mathbf{x}}^2(\mathbf{p}) = \alpha_{\mathbf{p}} \sum_{\Psi_{\mathbf{p},q} \neq \emptyset} C_n^2(q) \int_{s_{\mathbf{p},q}^{\min}}^{s_{\mathbf{p},q}^{\max}} s^{5/3} ds = \frac{3\alpha_{\mathbf{p}}}{8} \sum_{\Psi_{\mathbf{p},q} \neq \emptyset} C_n^2(q)[(s_{\mathbf{p},q}^{\max})^{8/3} - (s_{\mathbf{p},q}^{\min})^{8/3}] \qquad (9)$$

where

$$\alpha_{\mathbf{p}} = \frac{2.914 f^2}{D^{1/3} L_{\mathbf{p}}^{5/3} \cos^4(\text{AOA}_{\mathbf{p}})}. \qquad (10)$$

Here $L_{\mathbf{p}}$ is the length of $\text{LOS}_{\mathbf{p}}$ and $\text{AOA}_{\mathbf{p}}$ is the AOA of pixel $\mathbf{p}$. Let N_{pixels} be the total number of pixels in all viewpoints. Define a $N_{\text{pixels}} \times N_{\text{voxels}}$ matrix $\mathbf{A}$, whose element (p, q) is

$$A(k,q) = \begin{cases} 0 & \text{if } \Psi_{\mathbf{p},q} = \emptyset \\ \frac{3\alpha_{\mathbf{p}}}{8}[(s_{\mathbf{p},q}^{\max})^{8/3} - (s_{\mathbf{p},q}^{\min})^{8/3}] & \text{otherwise} \end{cases}. \qquad (11)$$

Matrix $\mathbf{A}$ is sparse. Column-stack the measured $\sigma_{\mathbf{x}}^2(\mathbf{p})$ to vector $\mathbf{m}$. Column-stack the unknown $C_n^2(k)$ to vector $\mathbf{c}$. Then, Eqs. (9,11) can be posed in vector form as

$$\mathbf{m} = \mathbf{A}\mathbf{c}. \qquad (12)$$

This linear system of equations can be solved by any standard solver. For example, it may be possible to use constrained and/or regularized least-squares:

$$\hat{\mathbf{c}} = \arg\min_{\mathbf{c}} \left(\|\mathbf{m} - \mathbf{A}\mathbf{c}\|^2 + \lambda\|\nabla^2 \mathbf{c}\|^2 \right) \qquad \text{s.t. } \mathbf{c} \geq \mathbf{0}, \qquad (13)$$

where λ weights a spatial smoothness regularizing term. When $\mathbf{A}$ is large, we use the Simultaneous Algebraic Reconstruction Technique (SART) [12] as the solver. Other priors [19], such as sparsity or a parametric form of $\mathbf{c}$ can also be used.

4   Simulation

We simulated volumetric distributions of C_n^2 as mixtures of 3D spatial Gaussians surrounded by 14 cameras across $70 \times 20 \times 70$ voxels. The cameras captured simulated pixel displacement variances, to which white Gaussian noise of standard deviation 0.05 pixels was added. We examined the reconstruction as a function

---

[2] We used the ray tracing algorithm from [5].
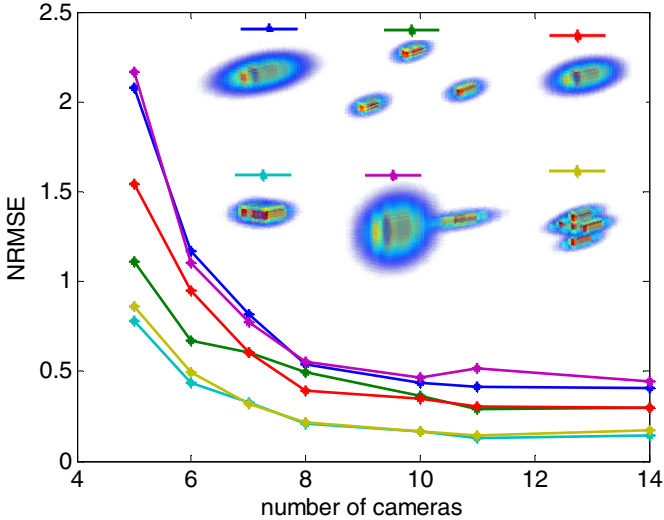
Fig. 5. Simulation results, for various simulated distributions of TS. NRMSE is plotted versus the number of cameras.

of the number of views considered, as shown in Fig. 5. The normalized root mean squared error (NRMSE)

$$\text{NRMSE} = \frac{\sqrt{\langle (\hat{C}_n^2 - C_n^2)^2 \rangle_{\mathbf{x}}}}{\max_{\mathbf{x}}(C_n^2)} \tag{14}$$

is plotted as a function of the number of cameras. Here $\hat{C}_n^2$ is the estimated TS while C_n^2 is the true simulated TS. We used the Laplacian operator with $0.01 \leq \lambda \leq 0.6$ with low values for large number of cameras and high values for small number of cameras. As the number of viewpoints increases, the recovery error drops. Errors are larger for large blobs and vice versa, as typical in tomography.

In addition, we compared two cases: a set of cameras forming a 360° circle versus 180° half circle. A 360° setting yields a smaller error, for the same number of cameras. This is expected, given the directional sensitivity described in Sec. 3.

5   Experiments

5.1   Laboratory

The experimental setup is shown in Fig. 6[Left]. Cooking stoves (Brentwood TS-322 1000W) produced heat, similarly to [44]. We used 11 stoves as shown in Fig. 6[Left]. Hot air from the stoves results in turbulence above the griddles.
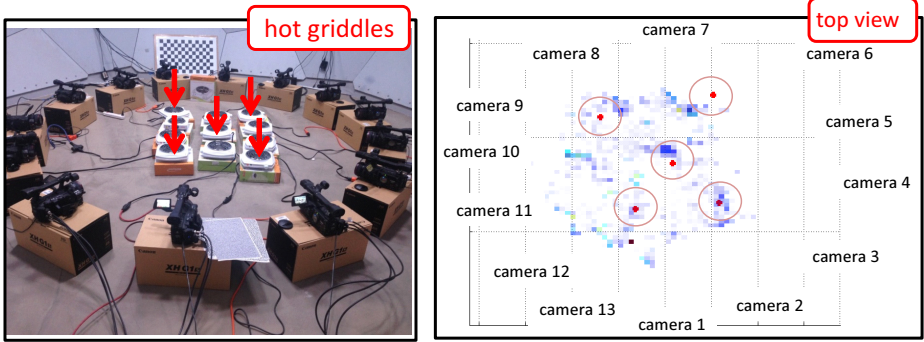
Fig. 6. [Left] Laboratory experimental setup. Multiple cameras encircle hot electric cooking stoves which create turbulence. Sample variance images from different viewpoints are shown in Fig. 3. [Right] Top view of an estimated C_n^2. Red dots indicate the true locations of hot operating stoves. Camera locations are also shown.

Various turbulence fields can be generated by individually controlling the power of each stove and its location. As background we placed a high frequency texture pattern [8], shown at the top of Fig. 3. Thirteen camcorders[3] observed the shimmering of the background through the turbulence field, at 30 fps. The cameras were calibrated using the method described in [49].

To use Eq. (12), $\mathbf{A}$ is derived by line integrals. We know the path length L from each camera to the pattern (Fig. 3[Top]). To compute the pixel displacement variance $\mathbf{m}$, we use dense optical flow [53] implemented in OpenCV. Sample variance images are shown in Fig. 3. Only voxels which are seen by most of the cameras are included in the reconstruction. Voxels that are not seen, or only seen by a few cameras, are excluded, similarly to the visual hull constraint as in [15]. The result of the estimated C_n^2 is shown in Fig. 6[Right]. Red dots indicate the true 3D location of stoves that were on during the experiment. Notice "hot-spots" of the estimated C_n^2 in the vicinity of the hot stoves.[4]

5.2   Outdoors

The outdoor experiment took place on a sunny day around noon, from 11:00AM until 2:30PM. Around noon, atmospheric turbulence should be the strongest and stationary over several hours [54]. The scene is Haifa Bay area. It is a valley with major industrial facilities interleaved by agricultural areas and some towns. Specifically, the area includes oil refineries with a lot of chimneys. In addition, Haifa Bay includes a port, an airport and a power station. Refer to Fig. 7 for a sketch map of the area. We used a Nikon D7100 DSLR camera with a telephoto

---

[3] The cameras are Canon HS-G1s high definition (HD), with F#=3.2 and exposure time 1/180 sec.

[4] The location of the hot stoves was estimated based on stereo triangulation using two cameras.
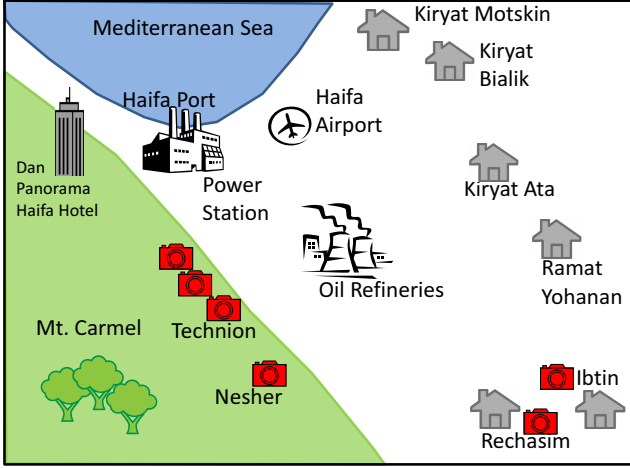
Fig. 7. Map of the Haifa Bay area. It has a valley which includes coastal suburbs (Kiryat Haim, Kiryat Motzkin and Kiryat Bialik), agricultural zones and heavy industry. The valley is surrounded by higher terrain, including Mt. Carmel (Technion, the cities of Haifa and Nesher) and hilly towns (Kfar Hasidim, Rechasim, Ibtin, Kiryat Ata). Red cameras mark locations from which we took image sequences during an experiment.

lens of $f = 300$mm, $F\# = 14$ and exposure time of 1/600sec. To gain a wide field of view (FOV), multiple narrow FOV videos were collected. We shot 30fps HD videos of ≈ 100 temporal frames for each narrow FOV. The scene was imaged from six viewpoints on the surrounding hills (see the red cameras in 7). The location of each view was recorded using GPS. Sample images of views and a stitched panorama are shown in Fig. 8.

To compute the line integrals in **A**, the locations of various scene objects in the images must be known. We used Google maps to locate the coordinates of multiple known landmarks in the valley landscape. We located, overall, 360 landmarks across all views. Fig. 9[Left] depicts the outdoor experimental setup. The rays to the known landmarks are shown by blue lines. The GPS Coordinates (latitude, longitude) were converted to local navigation coordinates (north, east, up) relative to the camera position in view 2. Our reconstruction area is essentially the area where rays cross.

Then, pixel displacement statistics (mean and variance) were computed for these landmarks in each temporal sequence of frames. The Kanade-Lucas-Tomasi (KLT) [25,45] algorithm implemented in Matlab was used for tracking corner points. The variance of each trajectory was computed to construct the vector **m**. The reconstruction area was divided into $20 \times 20 \times 1$ voxels. The estimated turbulence strength parameter (C_n^2) is shown in Fig. 9[Right] as a 2D map. We used the Laplacian regularization with $\lambda = 0.4$. The positions of the cameras are overlaid in green. Notice that a region with strong turbulence was estimated as the refineries plant ($C_n^2 = 1.7 \cdot 10^{-14} \ m^{-2/3}$). The second-strongest hot-spot
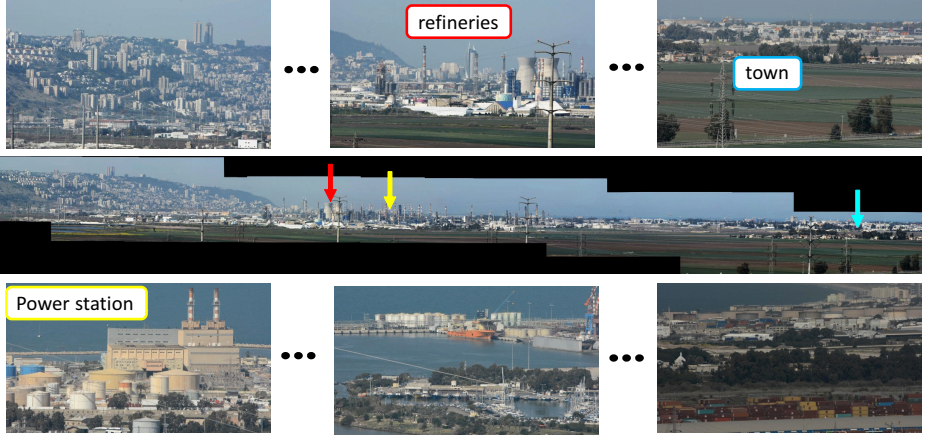
Fig. 8. Sample images from an outdoor experiment. Images of different views are shown. Places of interest are indicated on the images and also on the panorama. [Middle] The panorama image of view-2 was created using Microsoft image composite editor.
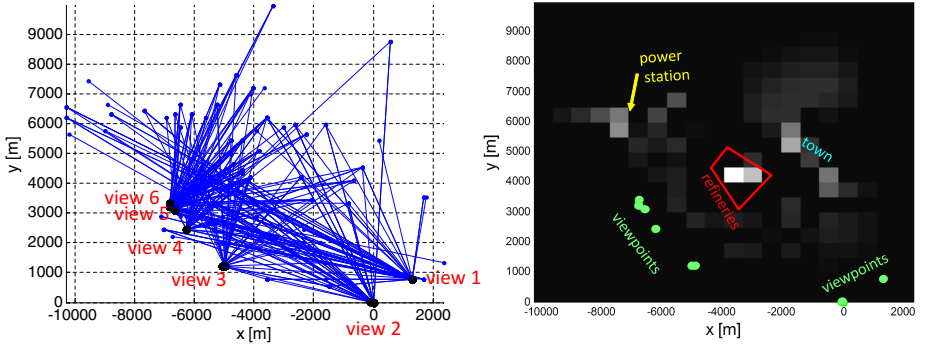
Fig. 9. [Left] Experimental setup of the outdoor experiment. Black dots indicate viewpoints. Any blue line represents a ray between a viewpoint and an object point. Figure axes are aligned to the compass cardinal directions in our region. [Right] The estimated TS parameter C_n^2 shown in a 2D map. Bright areas represent high values while dark areas represent low values. Regional places of interest are overlayed on the map. Notice the hottest spot is at the oil refineries.

was near the power station ($C_n^2 = 0.45 \cdot 10^{-14}\ m^{-2/3}$). A third, diffuse turbulent region was the town of Kiryat Ata. The agricultural fields around the refineries have weak turbulence. This agrees with our expectations.

6   Discussion

We describe a passive approach for estimating the volumetric spatially varying turbulence-strength field. As the approach does not require synchronization

between instruments, it can use simple hardware deployed in a wide range of scales. In contrast to a laboratory scenario, the outdoor experiment had no ground truth to validate. However, the results appear reasonable, at least qualitatively, based on the known landmarks in the valley. To quantitatively validate outdoor results, the estimated TS field might be compared to measurements using lidars and scintillators. More broadly, webcams observe cities worldwide, some over long ranges [23]. Their locations and viewing directions [24] can be used with our framework for potentially large-scale turbulence measurements.

References

1. Aides, A., Schechner, Y.Y., Holodovsky, V., Garay, M.J., Davis, A.B.: Multi sky-view 3D aerosol distribution recovery. Optics Express 21(22), 25820–25833 (2013)
2. Alterman, M., Schechner, Y.Y., Shamir, J., Perona, P.: Detecting motion through dynamic refraction. IEEE TPAMI 35, 245–251 (2013)
3. Alterman, M., Schechner, Y.Y., Swirski, Y.: Triangulation in random refractive distortions. In: Proc. IEEE ICCP (2013)
4. Alterman, M., Swirski, Y., Schechner, Y.: STELLA MARIS: Stellar marine refractive imaging sensor. In: Proc. IEEE ICCP (2014)
5. Amanatides, J., Woo, A.: A fast voxel traversal algorithm for ray tracing. Eurographics 87(3), 3–10 (1987)
6. Atcheson, B., Heidrich, W., Ihrke, I.: An evaluation of optical flow algorithms for background oriented Schlieren imaging. Experiments in Fluids 46(3), 467–476 (2009)
7. Atcheson, B., Ihrke, I., Heidrich, W., Tevs, A., Bradley, D., Magnor, M., Seidel, H.P.: Time-resolved 3D capture of non-stationary gas flows. ACM TOG 27(5), 132:1–132:9 (2008)
8. Couture, V., Martin, N., Roy, S.: Unstructured light scanning to overcome interreflections. In: Proc. IEEE ICCV, pp. 1895–1902 (2011)
9. Engelmann, R., Wandinger, U., Ansmann, A., Müller, D., Žeromskis, E., Althausen, D., Wehner, B.: Lidar observations of the vertical aerosol flux in the planetary boundary layer. J. Atmospheric & Oceanic Tech. 25(8), 1296–1306 (2008)
10. Gilles, J., Dagobert, T., De Franchis, C.: Atmospheric turbulence restoration by diffeomorphic image registration and blind deconvolution. In: Blanc-Talon, J., Bourennane, S., Philips, W., Popescu, D., Scheunders, P. (eds.) ACIVS 2008. LNCS, vol. 5259, pp. 400–409. Springer, Heidelberg (2008)

11. Gupta, M., Narasimhan, S.G., Schechner, Y.Y.: On controlling light transport in poor visibility environments. In: Proc. IEEE CVPR (2008)
12. Hansen, P.C., Saxild-Hansen, M.: AIR tools MATLAB package of algebraic iterative reconstruction methods. J. Computational and Applied Mathematics 236(8), 2167–2178 (2012)
13. Hargather, M.J., Settles, G.S.: Natural-background-oriented schlieren imaging. Experiments in Fluids 48(1), 59–68 (2010)
14. Harmeling, S., Hirsch, M., Sra, S., Schölkopf, B.: Online blind deconvolution for astronomy. In: Proc. IEEE ICCP (2009)
15. Ihrke, I., Magnor, M.: Image-based tomographic reconstruction of flames. In: Proc. ACM/EG Sympos. on Animation, pp. 367–375 (2004)
16. Ihrke, I., Goidluecke, B., Magnor, M.: Reconstructing the geometry of flowing water. In: Proc. IEEE ICCV, vol. 2, pp. 1055–1060 (2005)
17. Ji, Y., Ye, J., Yu, J.: Reconstructing gas flows using light-path approximation. In: Proc. IEEE CVPR (2013)
18. Joshi, N., Cohen, M.F.: Seeing Mt. Rainier: Lucky imaging for multi-image denoising, sharpening, and haze removal. In: Proc. IEEE ICCP (2010)
19. Kaftory, R., Schechner, Y.Y., Zeevi, Y.Y.: Variational distance-dependent image restoration. In: Proc. IEEE CVPR (2007)
20. Kolmogorov, A.N.: Dissipation of energy in locally isotropic turbulence. Dokl. Akad. Nauk. SSSR 32, 16–18 (1941)
21. Kolmogorov, A.N.: The local structure of turbulence in incompressible viscous fluid for very large reynolds numbers. Dokl. Akad. Nauk. SSSR 30, 299–303 (1941)
22. Kopeika, N.S.: A System Engineering Approach to Imaging. SPIE Press (1998)
23. Lalonde, J.F., Efros, A.A., Narasimhan, S.G.: Webcam clip art: Appearance and illuminant transfer from time-lapse sequences. ACM TOG 28(5), 131:1–131:10 (2009)
24. Lalonde, J.F., Narasimhan, S.G., Efros, A.A.: What do the sun and the sky tell us about the camera? IJCV 88(1), 24–51 (2010)
25. Lucas, B., Kanade, T.: An iterative image registration technique with an application to stereo vision. IJCAI 81, 674–679 (1981)
26. Ma, C., Lin, X., Suo, J., Dai, Q., Wetzstein, G.: Transparent object reconstruction via coded transport of intensity. In: Proc. IEEE CVPR (2014)
27. Messer, H., Zinevich, A., Alpert, P.: Environmental sensor networks using existing wireless communication systems for rainfall and wind velocity measurements. IEEE Instrum. Meas. Mag., 32–38 (2012)
28. Morris, N., Kutulakos, K.: Dynamic refraction stereo. In: Proc. IEEE ICCV, vol. 2, pp. 1573–1580 (2005)
29. Narasimhan, S., Nayar, S.: Vision and the atmosphere. IJCV 48(3) (2002)
30. Narasimhan, S.G., Nayar, S.K., Sun, B., Koppal, S.J.: Structured light in scattering media. In: IEEE ICCV, vol. 1, pp. 420–427 (2005)
31. Oberlack, M., Peinke, J., Talamelli, A., Castillo, L., Hölling, M.: Progress in Turbulence Wind Energy IV. In: Proc. iTi Conf. in Turbulence (2010)
32. Ramlau, R., Rosensteiner, M.: An efficient solution to the atmospheric turbulence tomography problem using Kaczmarz iteration. Inverse Problems 28(9), 095004 (2012)
33. Richard, H., Raffel, M., Rein, M., Kompenhans, J., Meier, G.: Demonstration of the applicability of a background oriented Schlieren (BOS) method. In: Intl. Symp. on Applications of Laser Techniques to Fluid Mechanics, pp. 145–156 (2000)
34. Roggemann, M.C., Welsh, B.: Imaging Through Turbulence. CRC Press (1996)

35. Schechner, Y.Y.: A view through the waves. Marine Technology Society Journal 47, 148–150 (2013)
36. Schechner, Y.Y., Diner, D.J., Martonchik, J.V.: Spaceborne underwater imaging. In: Proc. IEEE ICCP (2011)
37. Schechner, Y., Narasimhan, S., Nayar, S.: Polarization-based vision through haze. Applied Optics 42(3), 511–525 (2003)
38. Sedlazeck, A., Koser, K., Koch, R.: 3D reconstruction based on underwater video from ROV Kiel 6000 considering underwater imaging conditions. In: Proc. IEEE OCEANS EUROPE (2009)
39. Settles, G.S.: Schlieren and Shadowgraph Techniques: Visualizing Phenomena in Transparent Media. Springer (2001)
40. Shimizu, M., Yoshimura, S., Tanaka, M., Okutomi, M.: Super-resolution from image sequence under influence of hot-air optical turbulence. In: Proc. IEEE CVPR (2008)
41. Swirski, Y., Schechner, Y.Y.: 3Deflicker from motion. In: Proc. IEEE ICCP (2013)
42. Tatarskii, V.: Wave Propagation in a Turbulent Medium. McGraw-Hill Books (1961)
43. Tian, Y., Narasimhan, S.G.: Seeing through water: Image restoration using model-based tracking. In: Proc. IEEE ICCV, pp. 2303–2310 (2009)
44. Tian, Y., Narasimhan, S., Vannevel, A.: Depth from optical turbulence. In: Proc. IEEE CVPR (2012)
45. Tomasi, C., Kanade, T.: Detection and tracking of point features. Carnegie Mellon University Technical Report CMU-CS-91-132 (1991)
46. Trifonov, B., Bradley, D., Heidrich, W.: Tomographic reconstruction of transparent objects. In: Proc. Eurographics Symposium on Rendering, pp. 51–60 (2006)
47. Vasudeva, G., Honnery, D.R., Soria, J.: Non-intrusive measurement of a density field using the background oriented Schlieren (BOS) method. In: Proc. Australian Conf. Laser Diagnostic in Fluid Mechanics & Combustion (2005)
48. Venkatakrishnan, L., Meier, G.E.A.: Density measurements using the background oriented Schlieren technique. Experiments in Fluids 37, 237–247 (2004)
49. Vo, M., Wang, Z., Pan, B., Pan, T.: Hyper-accurate flexible calibration technique for fringe-projection-based three-dimensional imaging. Opt. Express 20(15), 16926–16941 (2012)
50. Wetzstein, G., Raskar, R., Heidrich, W.: Hand-held schlieren photography with light field probes. In: Proc. IEEE ICCP (2011)
51. Wetzstein, G., Roodnick, D., Raskar, R., Heidrich, W.: Refractive shape from light field distortion. In: Proc. IEEE ICCV (2011)
52. Xue, T., Rubinstein, M., Wadhwa, N., Levin, A., Durand, F., Freeman, W.T.: Refraction wiggles for measuring fluid depth and velocity from video. In: Proc. ECCV (2014)
53. Zach, C., Pock, T., Bischof, H.: A duality based approach for realtime TV-L1 optical flow. In: Hamprecht, F.A., Schnörr, C., Jähne, B. (eds.) DAGM 2007. LNCS, vol. 4713, pp. 214–223. Springer, Heidelberg (2007)
54. Zamek, S., Yitzhaky, Y.: Turbulence strength estimation from an arbitrary set of atmospherically degraded images. JOSA A 23(12), 3106–3113 (2006)
55. Zhu, X., Milanfar, P.: Stabilizing and deblurring atmospheric turbulence. In: Proc. IEEE ICCP (2011)